Article

Fast charging of energy-dense lithium-ion batteries

Chao-Yang Wang[1,2✉], Teng Liu[1], Xiao-Guang Yang[1,3], Shanhai Ge[1], Nathaniel V. Stanley[2], Eric S. Rountree[2], Yongjun Leng[1] & Brian D. McCarthy[2✉]

Lithium-ion batteries with nickel-rich layered oxide cathodes and graphite anodes have reached specific energies of 250–300 Wh kg^{-1} (refs. [1,2]), and it is now possible to build a 90 kWh electric vehicle (EV) pack with a 300-mile cruise range. Unfortunately, using such massive batteries to alleviate range anxiety is ineffective for mainstream EV adoption owing to the limited raw resource supply and prohibitively high cost. Ten-minute fast charging enables downsizing of EV batteries for both affordability and sustainability, without causing range anxiety. However, fast charging of energy-dense batteries (more than 250 Wh kg^{-1} or higher than 4 mAh cm^{-2}) remains a great challenge[3,4]. Here we combine a material-agnostic approach based on asymmetric temperature modulation with a thermally stable dual-salt electrolyte to achieve charging of a 265 Wh kg^{-1} battery to 75% (or 70%) state of charge in 12 (or 11) minutes for more than 900 (or 2,000) cycles. This is equivalent to a half million mile range in which every charge is a fast charge. Further, we build a digital twin of such a battery pack to assess its cooling and safety and demonstrate that thermally modulated 4C charging only requires air convection. This offers a compact and intrinsically safe route to cell-to-pack development. The rapid thermal modulation method to yield highly active electrochemical interfaces only during fast charging has important potential to realize both stability and fast charging of next-generation materials, including anodes like silicon and lithium metal.

Electric vehicle (EV) batteries must possess high energy density and fast rechargeability. Next-generation batteries with high specific capacity anodes are expected to reach more than 350 Wh kg^{-1} (ref. [2]), which could increase cruise range to greater than 400 miles (Supplementary Fig. 1a). Whereas higher energy densities have long been pursued, fast charging has only recently received increased attention[3,4]. True fast charging batteries would have immediate impact; a conventional long-range EV with a 120 kWh pack requiring an hour to recharge could be replaced with an EV with a 60 kWh pack capable of 10-min fast charging while maintaining very similar travel time during long-distance trips (Supplementary Fig. 1b). As there are not enough raw minerals for every internal combustion engine car to be replaced by a 120 kWh-equipped EV, fast charging is imperative for EVs to go mainstream.

Battery fast charging must be evaluated by three metrics simultaneously: (1) charge time, (2) specific energy acquired and (3) cycle number under the fast charge condition. Lack of any of the three numbers is inadequate or misleading. Such a figure of merit plot compiling all literature data is displayed in Fig. 1. The automotive-acceptable zone comprises a rectangle in the upper-left corner as defined by 150 Wh kg^{-1} minimum energy acquired within 15 min, as set by the US Department of Energy[4]. The ideal target is 240 Wh kg^{-1} acquired energy (for example, charging a 300 Wh kg^{-1} battery to 80% state of charge (SOC)) after a 5 min charge with a more than 2,000 cycle lifetime in which every charge

is a fast charge. Figure 1a shows literature data in which cycle lifetime was more than 800, hence meeting the minimum automotive cycle life requirement; Fig. 1b shows batteries with a cycle lifetime of less than 800 and hence far from automotive acceptable.

An exhaustive literature search revealed only three groups of technologies meeting the minimum automotive cycle lifetime requirement. First are lithium titanium oxide batteries, which can survive more than 30,000 15C charge cycles; unfortunately, their less than 100 Wh kg^{-1} is not practical[5]. Also in this unsuitable regime are supercapacitors and 0–25% SOC flash charging of lithium-ion batteries (LiBs). The second group are all-solid-state lithium metal batteries (LMBs), which demonstrate outstanding energy density and a 1,000-cycle lifetime, but with slow charging times. The third group—including this report—has graphite anodes, with this report being the first of this group, to our knowledge, to enter the automotive-acceptable zone.

As the most widely used LiB anode material, graphite's low equilibrium potential (100 mV versus Li|Li$^+$) yields high energy densities at heightened lithium plating risk; this detrimental side effect during fast charging induces rapid capacity loss and safety risk. To avoid and/or minimize lithium plating while fast charging thick graphite anodes of energy-dense LiBs, one must enhance the electrochemical and transport processes, including electrolyte ion transport[6,7], Li insertion kinetics and solid-particle diffusion[8]. Figure 1a,b show

[1]Electrochemical Engine Center (ECEC) and Department of Mechanical Engineering, Pennsylvania State University, University Park, PA, USA. [2]EC Power, State College, PA, USA. [3]Present address: National Engineering Laboratory for Electric Vehicles, School of Mechanical Engineering, Beijing Institute of Technology, Beijing, China. ✉e-mail: cxw31@psu.edu; bmccarthy@ecpowergroup.com
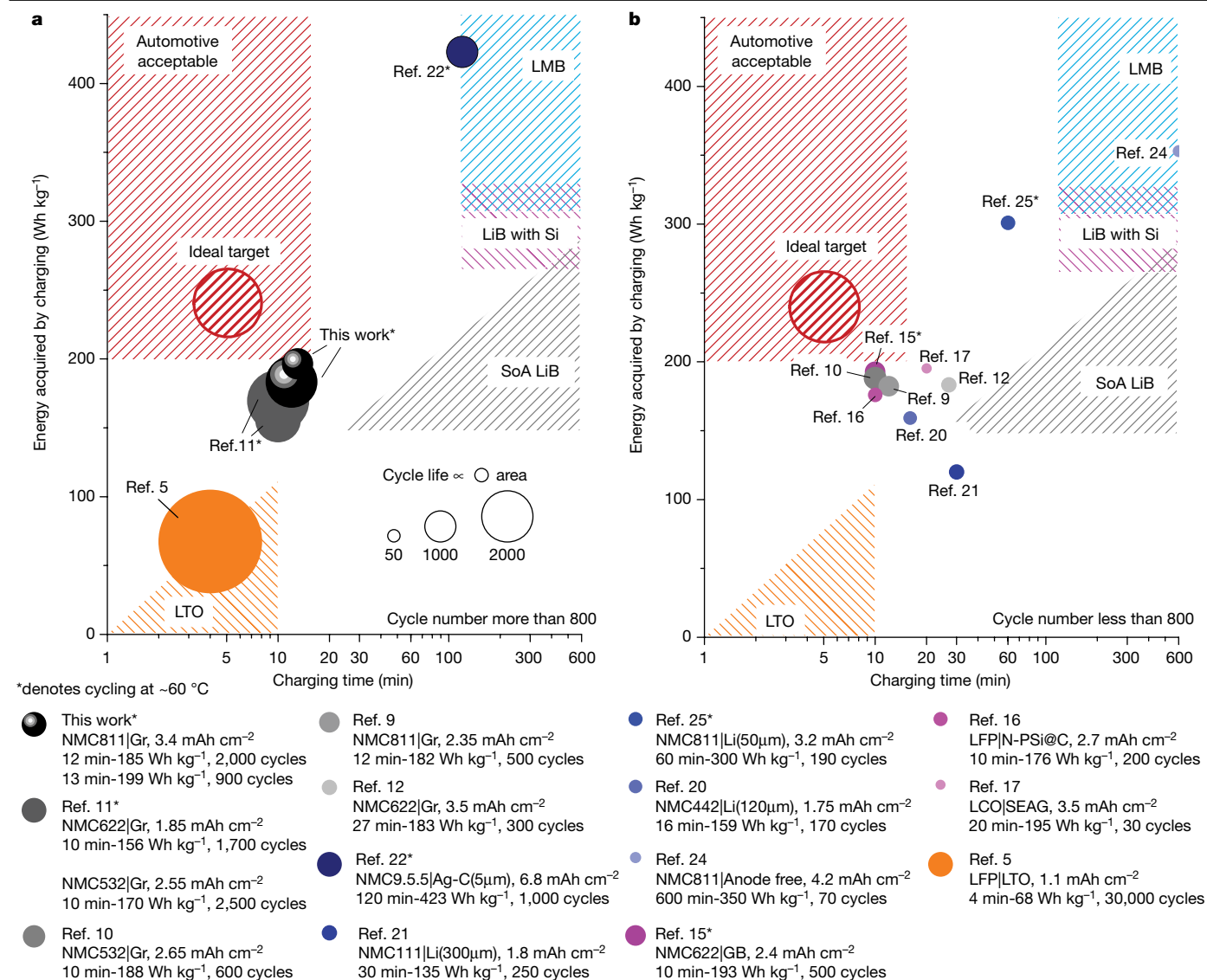
Fig. 1 | Figure of merit of fast charging batteries. A summary of literature studies on specific energy acquired by charging versus charge time, with the cycle life under a given charging condition displayed as the bubble size. Cell energy densities estimated using a 50 Ah cell design; see Supplementary Fig. 2. **a**, Cells with a cycle number of more than 800. **b**, Cells with a cycle number of less than 800. Data are from refs. [5,9–12,15–17,20–22,24,25].

examples in which these types of enhancement came close to being automotive-acceptable, achieved using alternative Li salts[9], decreased electrode tortuosity[10] or asymmetric temperature modulation (ATM)[11]. With one exception[12], previous fast-charging studies used 2–2.6 mAh cm^{-2} loadings, too low for EV batteries.

Alternative anodes are being aggressively researched; however, none is automotive-ready. Silicon anodes are promising[13], but their drastic volume expansion (more than 300%) during lithiation causes rapid capacity loss, especially during fast charging[14]. Intermediate approaches achieving usable cycle life and rate capability use lower silicon content[15–17]. In general, the calendar life of Si-anode batteries is still only 20–30 months, against the EV requirement of 100–140 months[18,19]. Lithium metal is another alternative anode, with some fast-charging results available[20–22]. However, LMBs capable of fast charging usually use thick lithium foils and excess electrolyte, resulting in low specific energies. The LMBs in Fig. 1 show a large gap from the automotive target[22–25].

Towards the goal of acquiring 240 Wh kg^{-1} by 15-min fast charging with more than 800 cycle life, herein we selected a LiNi$_{0.8}$Mn$_{0.1}$Co$_{0.1}$O$_2$ (NMC811) cathode with an areal capacity of 3.4 mAh cm^{-2} and cell-level specific energy of 265 Wh kg^{-1} in the 50 Ah format. By combining the ATM method with a dual-salt electrolyte and larger porosity anode for improved ion transport, we demonstrate an automotive-viable solution. The LiB lasted more than 900 cycles when charged at 4C to 75% SOC (about 250,000 miles), and around 2,000 cycles if the upper charge SOC was lowered to 70% (about 500,000 miles). This is a record-breaking combination of charge time, specific energy acquired and cycle life among all reported battery chemistries.

Asymmetric temperature modulation

The ATM method rapidly preheats the cell and then carries out fast charging at elevated temperatures to take advantage of thermally enhanced electrochemical and transport processes to eliminate lithium plating (Extended Data Fig. 1). After charging, the cell rapidly cools below 40 °C because of a large temperature difference driving fast heat dissipation[26]; the cell then rests and discharges around the ambient temperature as usual. Although ATM effectively eliminates lithium plating, its success hinges upon the notion that capacity degradation caused by the solid-electrolyte interphase (SEI) growth at elevated
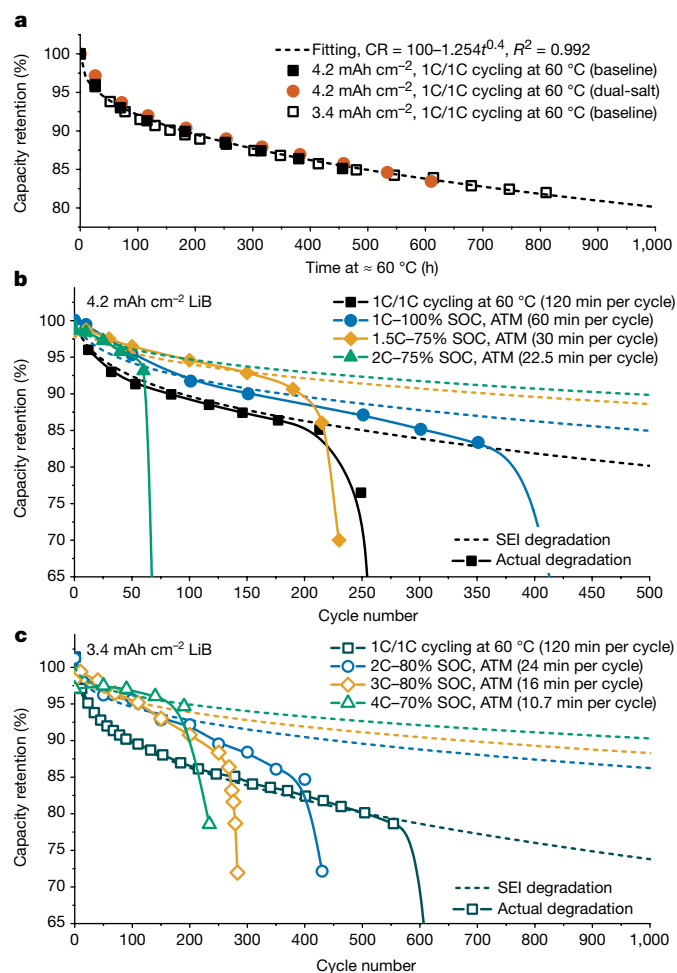
Fig. 2 | ATM cycles of energy-dense LiBs. a, Constant 1C/1C cycling at 60 °C to characterize SEI degradation. **b**, ATM fast charging of 4.2 mAh cm⁻² batteries at 1C, 1.5C and 2C to 100%, 75% and 75% SOC, respectively. **c**, ATM fast charging of 3.4 mAh cm⁻² batteries with the baseline electrolyte at 2C, 3C and 4C to 80%, 80% and 70% SOC, respectively. The solid lines in **b** and **c** denote the actual cell capacity loss, whereas the dashed lines represent the portion of SEI-caused degradation as calculated from the fitting equation derived from **a**. Deviation of a solid line from a corresponding dashed line thus represents the portion of capacity loss due to lithium plating. CR, capacity retention.

temperatures is a function of exposure time. Fortunately, such degradation is quite limited owing to the very short period of fast charging, as demonstrated in ref. [11]. In this work, we further innovate the concept using much higher energy-density cells of NMC811 cathode material with loadings of 3.4 and 4.2 mAh cm⁻² for two cell types. The anode material is artificial graphite and is matched to an NMC811 cathode with a negative to positive (N–P) capacity ratio of 1.1 in all cases. Two cell types were made (Supplementary Table 1a). First, baseline electrolyte cells had 1 M LiPF₆ in ethylene carbonate (EC)/ethyl methyl carbonate (EMC) (3:7 by weight) + 2 wt% vinylene carbonate. Second, dual-salt electrolyte cells had the same solvent and additive as the baseline, but with 0.6 M LiPF₆ and 0.6 M LiFSI.

Thermal stability was characterized by cycling each cell at 1C/1C at 60 °C and plotting capacity retention versus time at 60 °C (Fig. 2a). Two cells had thicker 4.2 mAh cm⁻² electrodes and either baseline or dual-salt electrolyte. A third cell had thinner 3.4 mAh cm⁻² electrodes and baseline electrolyte. The percent capacity retention versus cycle number for all three cells collapse onto a single curve, indicating that the SEI-caused cell degradation is indeed only a function of time as the specific surface area of graphite in both the thin and thick anodes is the same.

The dual salt used apparently does not change the SEI layer formation rate on the graphite anode; however, it did enhance electrolyte transport (Extended Data Fig. 2). The fitted curve in Fig. 2a provides a relation to calculate the capacity loss over time due to SEI degradation, clearly showing that batteries made of the present anode and cathode materials can survive at 60 °C for more than 1,000 h. If lithium plating could be fully eliminated during fast charging, this survival time would translate to thousands of extremely fast charging cycles (10–15 min per cycle) using the ATM method as the cells are at 60 °C only during preheating and fast charging.

The ATM cycling results of LiBs with areal loading of 4.2 mAh cm⁻² and 3.4 mAh cm⁻² are plotted in Fig. 2b,c; solid lines with symbols denote actual cell degradation, whereas dashed lines represent the SEI-only degradation as derived from Fig. 2a. Actual cell degradation initially follows the SEI-only calculated dashed line, indicative of no lithium plating. At a threshold number of cycles, the actual degradation (solid lines) deviates from its corresponding dashed line, signalling lithium plating onset. The nonlinear behaviour of cell ageing, also known as capacity rollover, is normally believed to be caused by either lithium plating[27–29] or cathode material impedance growth[30]. Here we find that capacity rollover occurs earlier when the areal capacities or charge currents become larger. Consequently, rollover is most probably caused by lithium plating as cathode instability should not be affected by the electrode areal capacity. Capacity rollover occurred earlier with faster charge rates (Fig. 2b,c), indicative of more severe lithium plating at higher C rates.

Comparing Fig. 2b with 2c shows that the less energy-dense LiB with an areal capacity of 3.4 mAh cm⁻² achieves higher cycle numbers and higher charge C rates before marked capacity rollover. Qualitatively consistent trends are also observed from the voltage relaxation diagnostics (Extended Data Fig. 3a,b). However, actual cycling results are more restrictive than the voltage relaxation diagnostics on fresh cells, probably because of the aggravated effect of ageing in the former cases[31]. Indeed, Extended Data Fig. 3a,b shows no evidence of notable lithium plating when the charge rate is less than 2C for a fresh 4.2 mAh cm⁻² cell or less than 4C for a fresh 3.4 mAh cm⁻² cell. However, the actual cycling results show that the 4.2 and 3.4 mAh cm⁻² cells cannot withstand higher than 1C and 1.5C charge rates, respectively. It is possible that, in continuously aged cells, lithium plating occurs later owing to degraded kinetics and mass transport properties. The deposited lithium metal will quickly react with the solvent, which further degrades the rate capability and accelerates new lithium metal deposition. This positive feedback mechanism accelerates capacity loss, which is also supported by a sudden drop in coulombic efficiency (Extended Data Fig. 3c,d) and a sharp increase of cell impedance (Extended Data Fig. 3e,f).

These parametric results show that 15-min/4C fast charging of energy-dense batteries without Li plating cannot be achieved with ATM alone; the electrolyte mass transport needs further enhancement. Indeed, among all the parameters involved in the charging process, ionic conductivity and ionic diffusivity have the lowest activation energy (10–20 kJ mol⁻¹) and attain the least improvement by temperature elevation[11,32].

Improved ionic transport

Electrolyte ionic transport through porous electrodes can be increased with better intrinsic properties (that is, higher ionic conductivity, higher ionic diffusivity and higher Li⁺ transference number) or by reducing the ratio of electrode tortuosity to porosity (MacMullin number)[8,33]. Here, we take both measures by using a LiPF₆–LiFSI dual-salt electrolyte and higher anode porosity.

Compared with LiPF₆, LiFSI has similar ionic conductivity (around 10 mS cm⁻¹ at 25 °C) and a higher transference number (0.56 versus 0.38 at 25 °C)[9,34,35] (Supplementary Fig. 3), and importantly is more thermally

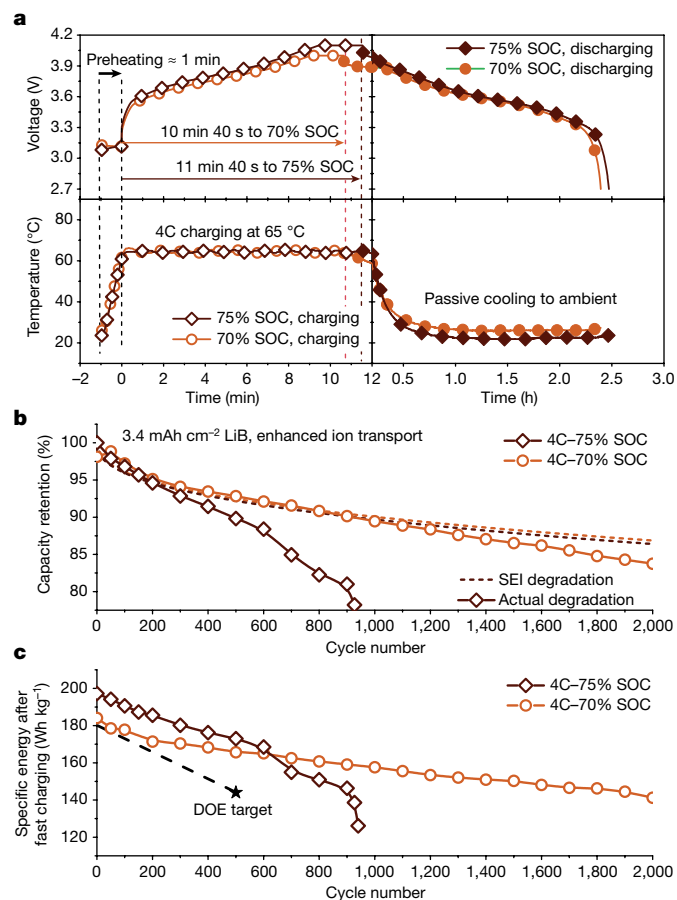**Fig. 3 | Fast charging of energy-dense LiBs with enhanced ion transport. a**, Voltage and temperature profiles for an ATM cycle. **b**, Capacity retention under fast charging. **c**, Specific energy acquired after fast charging.

stable. To leverage these properties, we switched to a dual-salt electrolyte in which 1 M LiPF$_6$ is replaced with 0.6 M LiFSI and 0.6 M LiPF$_6$. A remarkable improvement of high-rate performance results, with the relative capacity under 6C discharging increasing from 70% to 90% relative to the baseline electrolyte (Extended Data Fig. 2). Additionally, LiFSI's better thermal stability enables higher charging temperatures and so faster charging. A higher-porosity anode was also selected to reduce the tortuosity and MacMullin number based on the empirical relationship for graphite between porosity and MacMullin number[36]. Increasing the porosity from 0.26 to 0.35 increased the effective transport properties by 40% while decreasing the energy density by only 2% because of the need for more electrolyte (Supplementary Fig. 3b).

Fast charging energy-dense LiBs

Numerical modelling (Extended Data Fig. 4) and experimental voltage relaxation results (Extended Data Fig. 5) suggested that the new cell with the dual-salt electrolyte and higher porosity anode would have a maximum plating-free charge rate of 4C; this rate was used for experimental cycling tests. Two cells of 3.4 mAh cm^{-2} areal capacity were ATM cycled to either 70% or 75% SOC. Figure 3a illustrates voltage and temperature evolutions throughout the protocols. Before fast charging, the preheating step heated the cells from room temperature to 65 °C in around 1 min. Note that the preheating temperature was raised from 60 to 65 °C to further lower lithium plating risk. The cell temperature was maintained at roughly 65 °C during fast charging, which took about 11 min to reach 70% SOC and about 12 min to reach 75% SOC. Afterwards, the cells quickly cooled during C/3 discharge near room temperature.

Figure 3b displays the capacity retention data of both cycling tests, with dashed lines representing SEI-only degradation. When charging to 70% SOC, the actual cell degradation closely follows its calculated SEI-only degradation until approximately 1,200 cycles, indicating negligible lithium plating up to that point. The cell exceeded 2,000 cycles before reaching 20% capacity loss. This 265 Wh kg^{-1} battery could take 4C charging for more than 2,000 cycles; with the specific energy acquired by the fast charge reaching 184 Wh kg^{-1}, above the 180 Wh kg^{-1} DOE target (Fig. 3c). For the cell charged to 75% SOC, the capacity retention deviated from the solid line after about 300 cycles (Fig. 3b). The cell then aged linearly, with no capacity rollover before end of life. This translates to a cell with a 900 fast charge cycle life, with each charge acquiring about 200 Wh kg^{-1} (Fig. 3c).

Extended Data Figure 6 examines the cycling results of different experimental combinations of electrode and electrolyte design. The baseline LiB cycle life under 4C charging is about 200 cycles. If a single improvement is made—electrode or electrolyte—the cycle life only increases to 600–700 cycles. Only by combining a dual-salt electrolyte with high-porosity anodes was more than 2,000 cycles achieved, corresponding to a remarkable approximate 500,000 miles driven. These experimental findings and additional modelling studies (Extended Data Fig. 7) highlight that several strategies must be synergistically combined to break through current limitations for fast charging energy-dense batteries.

Charging at elevated temperatures may prove beneficial to decrease degradation of active materials other than graphite. For instance, at high charge rates, the concentration gradient within active material particles results in stress and irreversible particle cracking; this is believed to be a major NMC811 ageing mechanism[37]. Suppose instead that the battery is fast charged at elevated temperatures to yield improved solid-state diffusivity, reduced gradients, relief of particle strain and hence suppressed mechanical loss. The same methodology also applies to silicon, in which fast solid diffusion is necessary to reduce volume expansion-induced stress[38].

Pack cooling and safety

We next assessed the impact of an ATM strategy on cell cooling and safety at the pack level by building a digital 1/8-scale EV 12S1P pack model with aspirated air cooling based on the same 3.4 mAh cm^{-2}, high porosity electrodes used above in a 150 Ah prismatic cell format (Fig. 4a and Supplementary Table 2). This 12S1P model represents one module out of eight in a full pack, with all cooled equivalently. The cells are only air cooled on the top and bottom surfaces, with the faces tightly packed together. GT-AutoLion3D was used to perform electrochemical–thermal fully coupled simulations of the pack with the same electrochemical and electrode geometrical parameters from the validated one-dimensional (1D) model of Supplementary Table 3 and Extended Data Figs. 2 and 4. Pack simulations were carried out for the same cycle as in single cell testing (Fig. 3a): preheat to 65 °C, 4C charging to 75% SOC, 1 min rest and C/3 discharge.

The internal cell temperature distribution (Fig. 4b,c) was found to be quite uniform throughout the 4C charge and C/3 discharge owing to the much larger in-plane thermal conductivity (45.5 W m^{-1} K^{-1}) of electrode-separator stacks relative to the through-plane (0.55 W m^{-1} K^{-1})[39–41]. Cooling just the top and bottom surfaces with a heat transfer coefficient h = 140 W m^{-2} K^{-1}, accessible with forced air convection, was found to be sufficient to maintain battery temperature near 65 °C during 4C charging (Fig. 4c). In comparison, cooling of single cells (Fig. 3a) occurred under air natural convection with h less than 20 W m^{-2} K^{-1} because of the much larger surface area for heat dissipation. The simulations found that it took 11.6 min into the C/3 discharge for the cells to cool below 40 °C (Fig. 4c), close to the roughly 8 min observed in single-cell testing (Fig. 3a), and that this time could be reduced to around 5 min if air vents for aspirated convection were
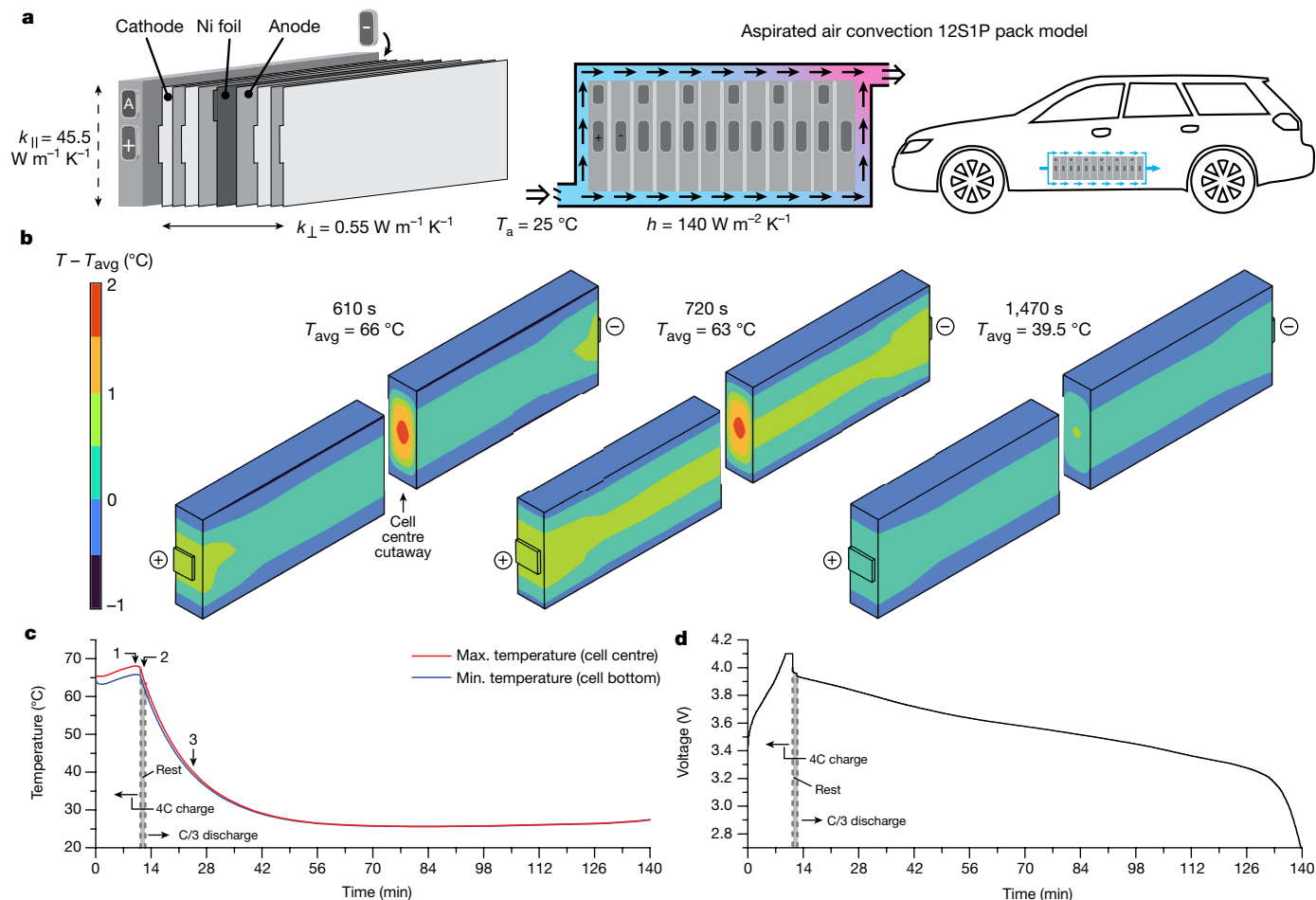
Fig. 4 | Electrochemical–thermal coupled simulations of a 12S1P pack of 150 Ah prismatic cells. a, Cell construction, pack model and thermal conditions under aspirated air convection. **b**, 3D temperature difference contours in 150 Ah prismatic cells at three representative time instants during 4C charge–C/3 discharge cycling. **c**, Evolution of maximum and minimum temperatures in the prismatic cell. **d**, Cell voltage evolution during cycling.

larger, for example increasing h to 300 W m⁻² K⁻¹ (Extended Data Fig. 8). These numerical results demonstrate the feasibility for ATM-enabled battery packs to achieve safe 4C charging while also replacing traditional liquid-refrigeration cooling with passive air thermal management. In practice, forced air convection could easily be implemented by installing a charger-powered fan, with cooling switching to aspirated air cooling during driving to reduce power consumption.

The safety of charging batteries at 65 °C is ensured by a combination of very short exposure to elevated temperatures and use of a more thermally stable lithium salt. The total elevated temperature exposure time amounts to 167 h (10 min per cycle) for 1,000 fast-charge cycles, only 0.167% of a 12-year electric vehicle lifetime. Indeed, capacity retention loss due to accelerated SEI degradation over 167 h is still much lower than the 20% total loss limit (Fig. 2a), implying no safety concerns. Recent work[42], appearing after our initial submission, showed that NMC/graphite cells could be safely cycled at 70 °C for 6 months with little ageing. A new perspective, also published after initial submission, concluded that intrinsically safe batteries of the future must be heat-tolerant and exhibit great resistance to thermal runaway[43]. Charging at elevated temperatures eliminates Li plating while also enhancing safety. Finally, we note that thermally modulated 4C charging requires only air convection from the bottom and top cell surfaces, permitting an intrinsically safe and reliable pack design. By contrast, traditional battery packs must resort to liquid cooling through sophisticated three-dimensional coolant channels, which are subject to intense squeezing from cell expansion upon ageing and are thus prone to coolant leakage.

Online content

Any methods, additional references, Nature Research reporting summaries, source data, extended data, supplementary information, acknowledgements, peer review information; details of author contributions and competing interests; and statements of data and code availability are available at https://doi.org/10.1038/s41586-022-05281-0.

1. Wu, Y. et al. An empirical model for the design of batteries. *ACS Energy Lett.* **5**, 807–816 (2020).
2. Deng, J., Bae, C., Denlinger, A. & Miller, T. Electric vehicles batteries: requirements and challenges. *Joule* **4**, 511–515 (2020).
3. Cheeseman, H. Fast-charging Li-metal batteries. *ARPA-E* https://arpa-e.energy.gov/open-2021/webinars (2021).
4. Howell, D. et al. Enabling fast charging: a technology gap assessment. *US Department of Energy* https://www.energy.gov/sites/default/files/2017/10/f38/XFC%20Technology%20Gap%20Assessment%20Report_FINAL_10202017.pdf (2017).
5. Zaghib, K. et al. Safe and fast-charging Li-ion battery with long shelf life for power applications. *J. Power Sources* **196**, 3949–3954 (2011).
6. Colclasure, A. M. et al. Electrode scale and electrolyte transport effects on extreme fast charging of lithium-ion cells. *Electrochim. Acta* **337**, 135854 (2020).
7. Logan, E. R. et al. Ester-based electrolytes for fast charging of energy dense lithium-ion batteries. *J. Phys. Chem. C* **124**, 12269–12280 (2020).
8. Liu, T., Yang, X., Ge, S., Leng, Y. & Wang, C. Y. Ultrafast charging of energy-dense lithium-ion batteries for urban air mobility. *eTransportation* **7**, 100103 (2021).
9. Du, Z., Wood Iii, D. L. & Belharouak, I. Enabling fast charging of high energy density Li-ion cells with high lithium ion transport electrolytes. *Electrochem. Comm.* **103**, 109–113 (2019).
10. Chen, K. et al. Efficient fast-charging of lithium-ion batteries enabled by laser-patterned three-dimensional graphite anode architectures. *J. Power Sources* **471**, 228475 (2020).

Article

11. Yang, X.-G. et al. Asymmetric temperature modulation for extreme fast charging of lithium-ion batteries. *Joule* **3**, 3002–3019 (2019).

12. Han, J.-G. et al. An electrolyte additive capable of scavenging HF and PF5 enables fast charging of lithium-ion batteries in LiPF6-based electrolytes. *J. Power Sources* **446**, 227366 (2020).

13. Gonzalez, A. F., Yang, N.-H. & Liu, R.-S. Silicon anode design for lithium-ion batteries: progress and perspectives. *J. Phys. Chem. C* **121**, 27775–27787 (2017).

14. Lee, S. K., McDowell, M. T., Choi, J. W. & Cui, Y. Anomalous shape changes of silicon nanopillars by electrochemical lithiation. *Nano Lett.* **11**, 3034–3039 (2011).

15. Son, I. H. et al. Graphene balls for lithium rechargeable batteries with fast charging and high volumetric energy densities. *Nat. Commun.* **8**, 1561 (2017).

16. Wang, B. et al. Ultrafast-charging silicon-based coral-like network anodes for lithium-ion batteries with high energy and power densities. *ACS Nano* **13**, 2307–2315 (2019).

17. Kim, N., Chae, S., Ma, J., Ko, M. & Cho, J. Fast-charging high-energy lithium-ion batteries via implantation of amorphous silicon nanolayer in edge-plane activated graphite anodes. *Nat. Commun.* **8**, 812 (2017).

18. McBrayer, J. D. et al. Calendar aging of silicon-containing batteries. *Nat. Energy* **6**, 866–872 (2021).

19. Masias, A., Marcicki, J. & Paxton, W. A. Opportunities and challenges of batteries in automotive applications. *ACS Energy Lett.* **6**, 621–630 (2021).

20. Zheng, J. et al. Electrolyte additive enabled fast charging and stable cycling lithium metal batteries. *Nat. Energy* **2**, 17012 (2017).

21. Peng, Z. et al. High-power lithium metal batteries enabled by high-concentration acetonitrile-based electrolytes with vinylene carbonate additive. *Adv. Funct. Mater.* **30**, 2001285 (2020).

22. Lee, Y.-G. et al. High-energy long-cycling all-solid-state lithium metal batteries enabled by silver–carbon composite anodes. *Nat. Energy* **5**, 299–308 (2020).

23. Niu, C. et al. High-energy lithium metal pouch cells with limited anode swelling and long stable cycles. *Nat. Energy* **4**, 551–559 (2019).

24. Ren, X. et al. Enabling high-voltage lithium-metal batteries under practical conditions. *Joule* **3**, 1662–1676 (2019).

25. Leng, Y. et al. Fast charging of energy-dense lithium metal batteries in localized ether-based highly concentrated electrolytes. *J. Electrochem. Soc.* **168**, 060548 (2021).

26. Liu, T., Ge, S., Yang, X.-G. & Wang, C.-Y. Effect of thermal environments on fast charging Li-ion batteries. *J. Power Sources* **511**, 230466 (2021).

27. Keil, J. et al. Linear and nonlinear aging of lithium-ion cells investigated by electrochemical analysis and in-situ neutron diffraction linear and nonlinear aging of lithium-ion cells investigated by electrochemical analysis and in-situ neutron diffraction. *J. Electrochem. Soc.* **166**, A3908 (2019).

28. Schuster, S. F. et al. Nonlinear aging characteristics of lithium-ion cells under different operational conditions. *J. Energy Storage* **1**, 44–53 (2015).

29. Yang, X.-G., Leng, Y., Zhang, G., Ge, S. & Wang, C.-Y. Modeling of lithium plating induced aging of lithium-ion batteries: transition from linear to nonlinear aging. *J. Power Sources* **360**, 28–40 (2017).

30. Ma, X. et al. Hindering Rollover Failure of Li[Ni0.5Mn0.3Co0.2]O2/Graphite Pouch Cells during Long-Term Cycling. *J. Electrochem. Soc.* **166**, A711 (2019).

31. Yang, X.-G., Ge, S., Liu, T., Leng, Y. & Wang, C.-Y. A look into the voltage plateau signal for detection and quantification of lithium plating in lithium-ion cells. *J. Power Sources* **395**, 251–261 (2018).

32. Ogihara, N. et al. Theoretical and experimental analysis of porous electrodes for lithium-ion batteries by electrochemical impedance spectroscopy using a symmetric cell. *J. Electrochem. Soc.* **159**, A1034–A1039 (2012).

33. Newman, J. S. & Tobias, C. W. Theoretical analysis of current distribution in porous electrodes. *J. Electrochem. Soc.* **109**, 1183 (1962).

34. Li, L. et al. Transport and electrochemical properties and spectral features of non-aqueous electrolytes containing LiFSI in linear carbonate solvents. *J. Electrochem. Soc.* **158**, A74 (2011).

35. Han, H.-B. et al. Lithium bis(fluorosulfonyl)imide (LiFSI) as conducting salt for nonaqueous liquid electrolytes for lithium-ion batteries: physicochemical and electrochemical properties. *J. Power Sources* **196**, 3623–3632 (2011).

36. Landesfeind, J., Hattendorff, J., Ehrl, A., Wall, W. A. & Gasteiger, H. A. Tortuosity determination of battery electrodes and separators by impedance spectroscopy. *J. Electrochem. Soc.* **163**, A1373–A1387 (2016).

37. Bi, Y. et al. Reversible planar gliding and microcracking in a single-crystalline Ni-rich cathode. *Science* **370**, 1313–1317 (2020).

38. Li, Y. et al. Growth of conformal graphene cages on micrometre-sized silicon particles as stable battery anodes. *Nat. Energy* **1**, 15029 (2016).

39. Yang, X.-G., Zhang, G. & Wang, C. Y. Computational design and refinement of self-heating lithium ion batteries. *J. Power Sources* **328**, 203–211 (2016).

40. Zhang, J., Wu, B., Li, Z. & Huang, J. Simultaneous estimation of thermal parameters for large-format laminated lithium-ion batteries. *J. Power Sources* **259**, 106–116 (2014).

41. Ye, Y., Saw, L. H., Shi, Y., Somasundaram, K. & Tay, A. A. O. Effect of thermal contact resistances on fast charging of large format lithium ion batteries. *Electrochim. Acta* **134**, 327–337 (2014).

42. Aiken, C. P. et al. Li[Ni0.5Mn0.3Co0.2]O2 as a superior alternative to LiFePO4 for long-lived low voltage li-ion cells. *J. Electrochem. Soc.* **169**, 050512 (2022).

43. Longchamps, R. S., Yang, X. G. & Wang, C. Y. Fundamental insights into battery thermal management and safety. *ACS Energy Lett.* **7**, 1103–1111 (2022).

Methods

Cell materials and fabrication

$LiNi_{0.8}Mn_{0.1}Co_{0.1}O_2$ (NMC811) and graphite were used as the cathode and anode materials for cell fabrication in this work. With different combinations of loadings and porosities, testing results coming from three types of electrode are presented. As shown in Supplementary Table 1, the 'Energy-dense+' cell had a mass loading of 21.3 mg cm^{-2} on the cathode side; this was matched with a 13.4 mg cm^{-2} anode to give a corresponding design capacity of 4.2 mAh cm^{-2}. For the cell with an areal capacity of 3.4 mAh cm^{-2}, the mass loadings were 17.2 mg cm^{-2} and 10.8 mg cm^{-2} for cathode and anode, respectively. Mass-produced industrial electrodes for high-energy LiBs usually have low porosity, which equalled 0.26 for the baseline cells in this study. A high porosity anode ($\varepsilon = 0.35$) is used to improve the mass transport in the electrolyte phase during fast charging, while the porosity in the cathode is kept at 0.3 for all the cells. The electrolytes used in this study had two formulas. The baseline electrolyte consisted of 1 M LiPF$_6$ dissolved in EC/EMC (3:7 by weight) + 2 wt% vinylene carbonate. The dual-salt electrolyte used the same solvent and additive as the baseline, but the salt was replaced by 0.6 M LiFSI and 0.6 M LiPF$_6$. The test pouch cells were fabricated in 3–5 Ah formats to demonstrate the cell-level performance. For actual cells used in EV applications, the capacity can reach more than 50 Ah (ref. [44]). If we use a 50 Ah design to evaluate the specific energy of the cells, it could reach 283 Wh kg^{-1} when using high loading electrodes of 4.2 mAh cm^{-2}. Under an areal capacity of 3.4 mAh cm^{-2}, the specific capacity of the cell comes to 271 Wh kg^{-1}; if a high porosity anode is adopted, then the specific capacity becomes 265 Wh kg^{-1}.

The cells fabricated for ATM cycling had an embedded Ni foil for preheating; the 27-μm-thick foil was coated with polyethylene terephthalate (total weight was 1.5% of the battery mass) and placed inside the cell[45]. The internal self-heating structure enables rapid heating of LiBs with heating rates up to 1 °C s^{-1} while maintaining a good temperature uniformity regardless of the cell format[46].

Cycling tests

Cycling tests were done with an Arbin Instruments BT2000. For thermal stability characterization, the cells were placed in a 60 °C environment chamber, cycled under 1C CCCV charging (4.15 cut-off voltage, C/3 cut-off current) and followed by a 1C discharge to 2.7 V. ATM cycling tests were conducted in the 20 °C ambient and comprised a preheating step, fast charging step (with internal heating turned off) and a discharge step. We achieved preheating with an internal heating element made of a 30-μm-thick nickel foil embedded in the centre electrode layers[45], which only weighs 1.5% that of the cell. As shown in Extended Data Fig. 1a, the heating sheet has two terminals; one end is connected to the negative terminal of the cell, and the other end is extended from the cell and forms a third terminal called the activation terminal. Extended Data Figure 1b shows the evolution of cell temperature during heating. When applying a 3.3 V voltage (around the open circuit voltage of the discharged battery) to the heating element, we can get a heating rate of 0.75 °C s^{-1}, that is, heating a cell from room temperature to 60–65 °C within 1 min. The maximum temperature difference between the heater surface and cell outer surface is roughly 10 °C during preheating and diminishes to around 1 °C, 10 s after preheating ceases. Here the cell outer surface temperature was measured with a thermocouple, and the internal heater temperature was back-calculated from the foil resistance based on a precalibrated linear relationship[47].

The cell starts charging after reaching a target charge temperature. The charging process uses a CCCV protocol; the cut-off current equalled half of the CC charging current, and the charge step terminates either when the target SOC or the cut-off current is reached. The target SOCs ranged from 70% to 80% in different tests, and the cut-off voltage was also adjusted to match the target SOCs, that is, under target SOCs of 80%, 75% and 70%, the cut-off voltages were 4.15 V, 4.1 V and 4.0 V, respectively.

Once the high-current charging ceases, the large internal heat generation vanishes, and the battery temperature drops close to ambient within several minutes and continues during the discharge step.

Electrochemical–thermal model

Commercial software, GT-AutoLion in 1D (for single cells) and 3D (for packs) versions, was used to solve the physics-based ECT model (governing equations shown in the Supplementary Information equations (S1)–(11)); an identical 1D model was used in our earlier study[26]. The modelling parameters used in this work are summarized in Supplementary Table 2, and comparison of the model's results with experimental data is shown in Extended Data Figs. 2 and 4. The occurrence of lithium plating is determined by Supplementary Information equation (12).

Electrochemical impedance spectroscopy

The electrochemical impedance spectroscopy (EIS) tests were conducted with a Solatron ModuLlab Xm. The cells were held at 3.96 V (approximately 80% SOC) for more than 2 h before the tests. A signal with 2 mV amplitude was applied to the cell with a frequency sweep from 10 kHz to 0.01 Hz. The impedance in the complex plane has a similar shape to the equivalent circuit depicted in Extended Data Fig. 9a. The impedance at different frequencies corresponds to different electrochemical processes in the battery. The high-frequency resistance is set to be the resistance at 1 kHz, which comes from the contact resistance, the ohmic resistance in the solid phase of electrodes and the ohmic resistance of electrolyte that fills the pores of the electrodes and separators. At low frequency, the impedance in the complex plane shows a straight line with roughly a 45° phase angle, which is known as the Warburg element (semi-infinite), Z_W, describing the diffusion process in solid particles. In between, the semicircles correspond to the charge transfer process at different reaction interfaces, and the resistance of this segment is known as the charge transfer resistance, R_{ct}.

An equivalent circuit with four components is used to fit and interpret the results of the EIS tests[48]. The details of the equivalent circuit and the derivation of fitting expression (Supplementary equations (13)–(18)) are given in the Supplementary Information.

Data availability

All data generated or analysed during this study are included in this published article, the Extended Data and the Supplementary Information.

44. Lima, P. Samsung SDI 94 Ah battery cell full specifications. *PushEVs* https://pushevs.com/2018/04/05/samsung-sdi-94-ah-battery-cell-full-specifications/ (2021).
45. Wang, C. Y. et al. Lithium-ion battery structure that self-heats at low temperatures. *Nature* **529**, 515–518 (2016).
46. Yang, X. G., Liu, T. & Wang, C. Y. Innovative heating of large-size automotive Li-ion cells. *J. Power Sources* **342**, 598–604 (2017).
47. Zhang, G. et al. Rapid self-heating and internal temperature sensing of lithium-ion batteries at low temperatures. *Electrochim. Acta* **218**, 149–155 (2016).
48. Leng, Y. et al. Electrochemical cycle-life characterization of high energy lithium-ion cells with thick Li(Ni0.6Mn0.2Co 0.2)O2 and graphite electrodes. *J. Electrochem. Soc.* **164**, A1037–A1049 (2017).

Author contributions C.Y.W., T.L., B.D.M. and E.S.R. wrote the manuscript. S.G. designed and built the cells. T.L. and X.G.Y. designed the experiments. T.L. built the test stand and carried out the experiments. Y.L. optimized electrolytes in coin cells. C.Y.W., N.V.S. and B.D.M. designed and performed 3D numerical simulations. All authors contributed to development of the manuscript and to discussions as the project developed.

a

b
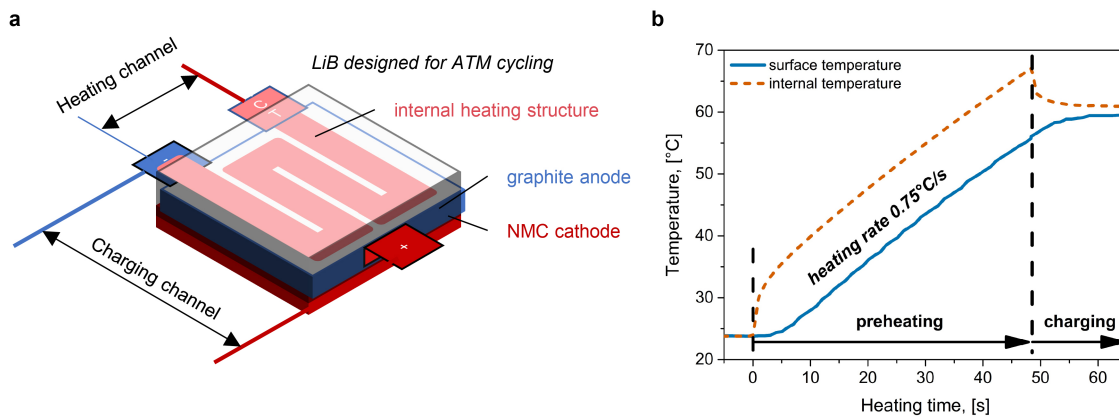
Extended Data Fig. 1 | LiB design for ATM cycling. a, LiB with an embedded nickel foil for internal heating. Before each charging, current goes through the internal heating structure and heats up the cell to 65 °C in less than one minute. After reaching the target temperature, the charging channel starts to take in energy and maintains thermal balance throughout the charging process. **b**, Cell and heating-foil temperatures versus heating time. A heating rate of 0.75 °C s⁻¹ was achieved when applying 3.3 V on the heating channel.
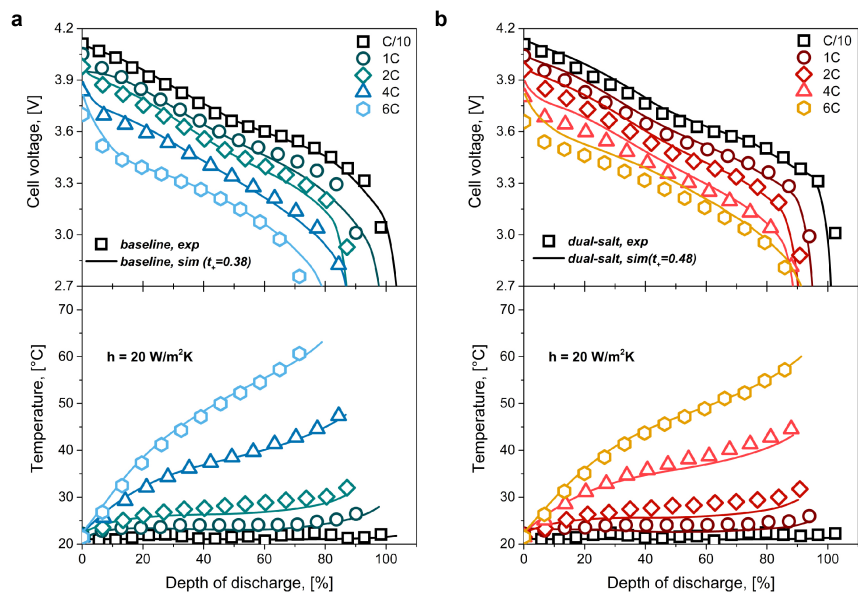
Extended Data Fig. 2 | Rate performance tests and model validation. a, Cell with baseline electrolyte. **b**, Cell with dual-salt electrolyte; the simulated transference number was 0.48.
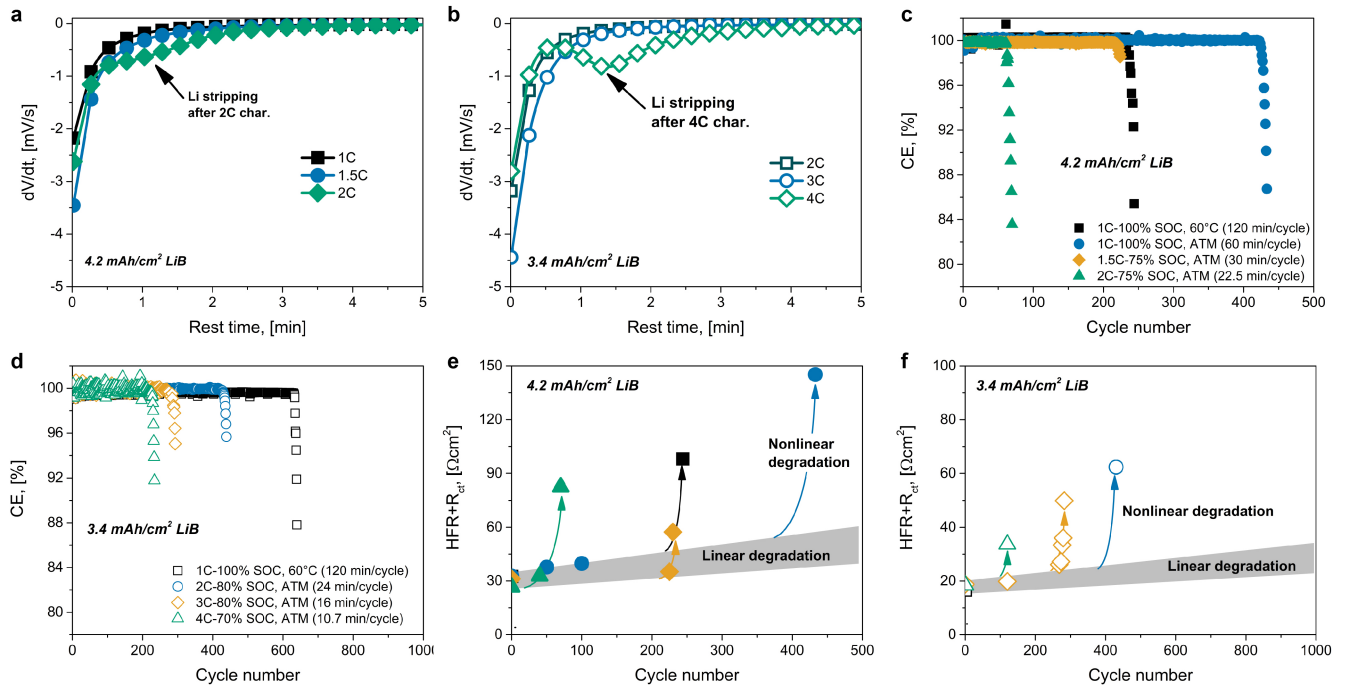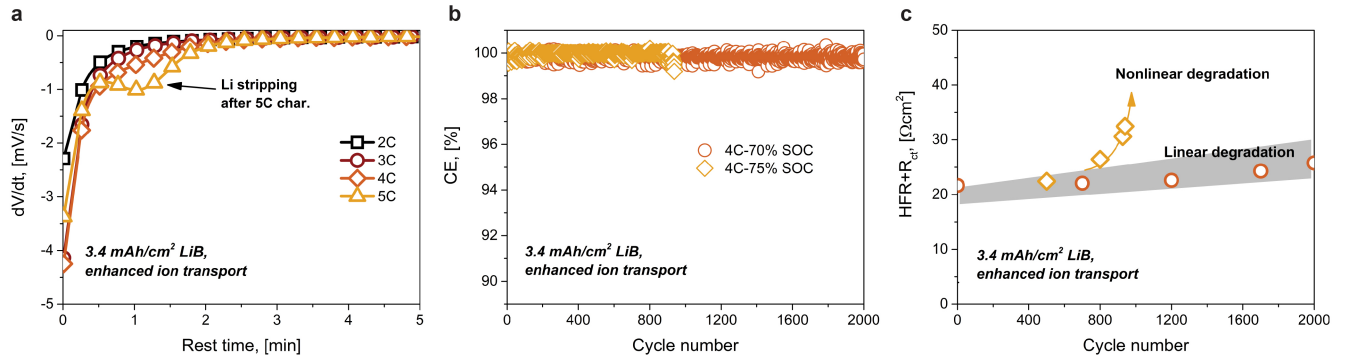
Extended Data Fig. 3 | Ageing mechanisms under ATM cycling. a, **b**, Lithium plating detection with voltage relaxation method for 4.2 mAh cm⁻² LiBs and 3.4 mAh cm⁻² LiBs. **c**, **d**, Coulombic efficiency during cycling. **e**, **f**, Change of resistance attained by EIS tests. Baseline electrolyte was used in these tests.
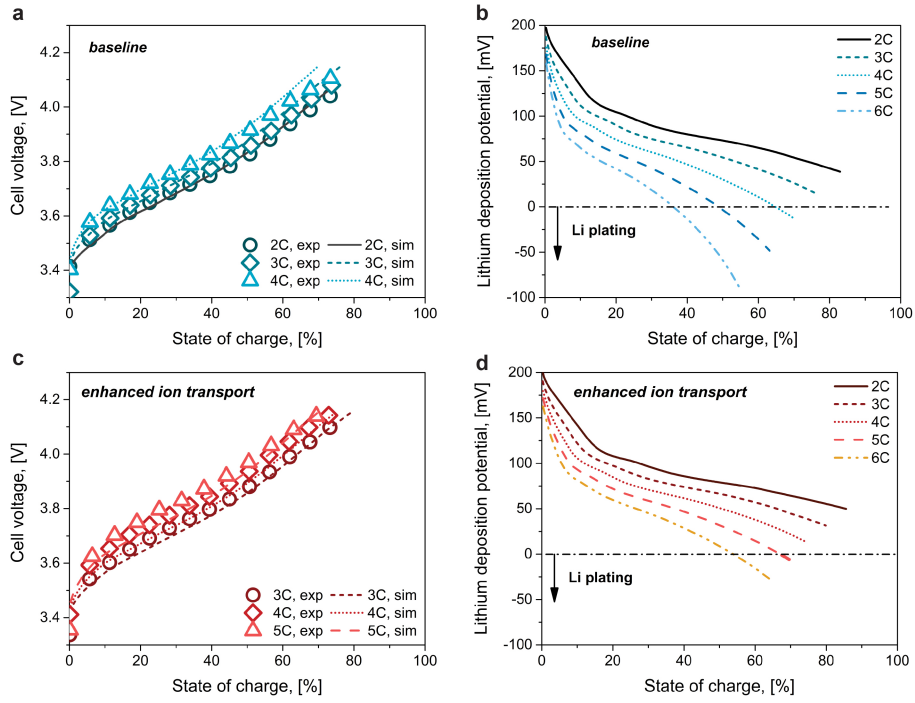
Extended Data Fig. 4 | Numerical prediction of lithium plating at various charge rates with *T*=60°C. a, Experimental and simulated voltage profiles for baseline cells. **b**, Simulated lithium deposition potential for baseline cells. **c**, Experimental and simulated voltage profiles for cells with dual-salt electrolyte. **d**, Simulated lithium deposition potential for cells with dual-salt electrolyte.

Extended Data Fig. 5 | Ageing mechanisms under fast charging of batteries with enhanced ion transport. a, Lithium plating detection with voltage relaxation method for 3.4 mAh cm^{-2} LiBs with enhanced ion transport. **b**, Coulombic efficiency during cycling. **c**, Change of resistance attained by EIS tests.
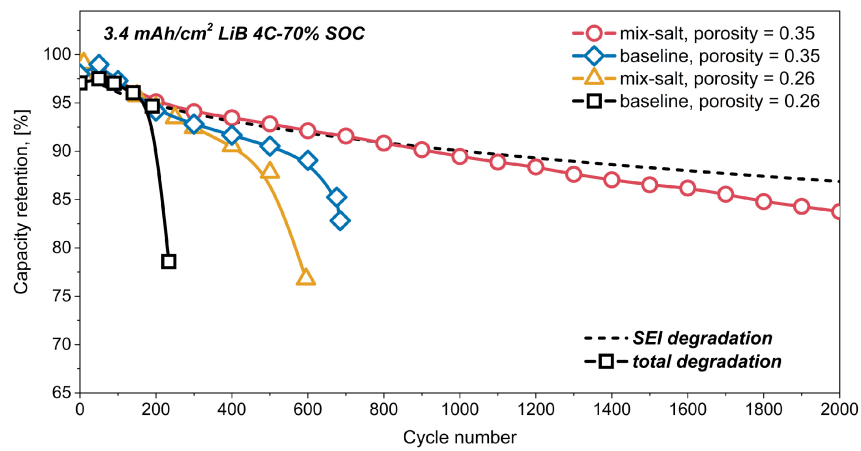
Extended Data Fig. 6 | Fast charging cycling with different combinations of electrodes and electrolytes. Use of either the mixed dual-salt electrolyte or higher porosity anodes failed to give long cycle lifetime; both were required for long cycle lifetime.
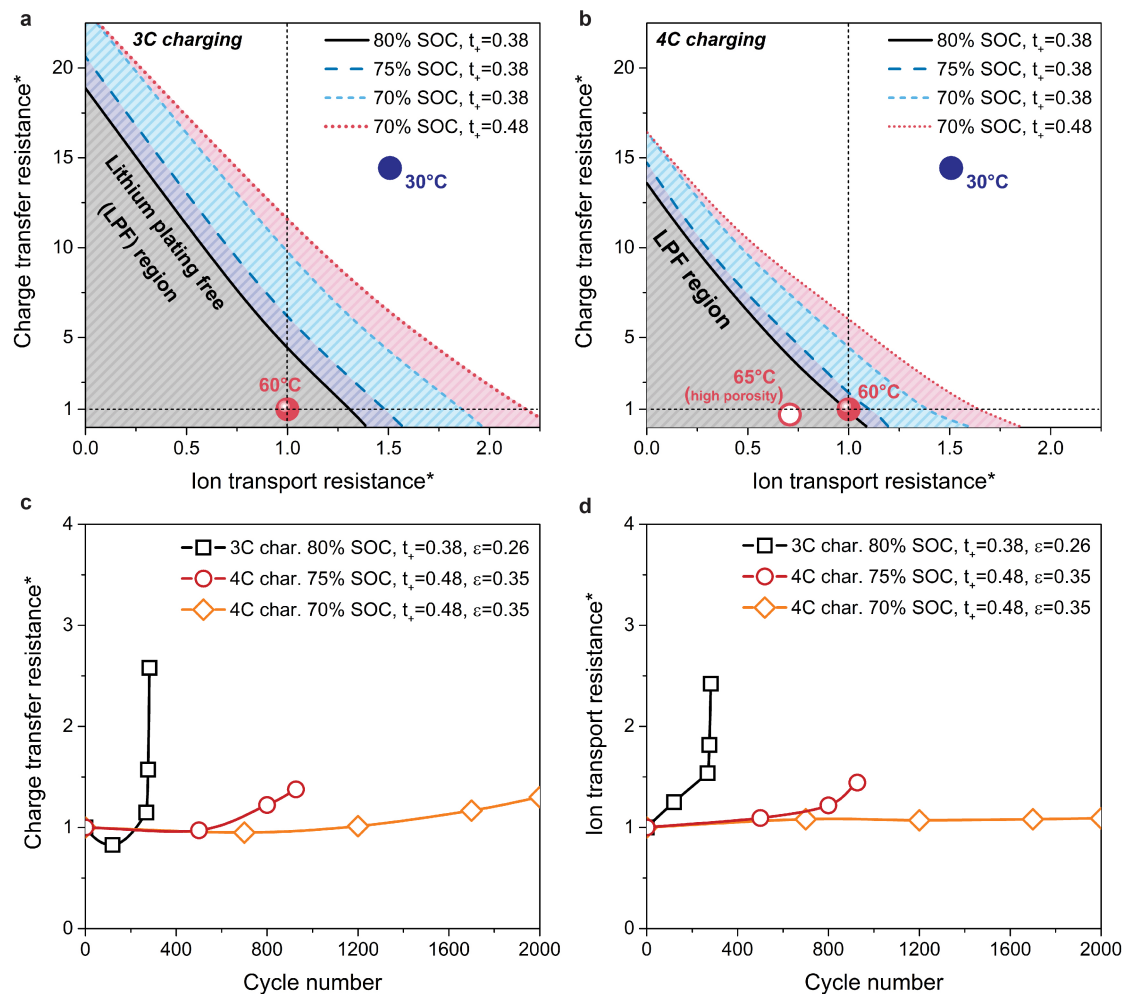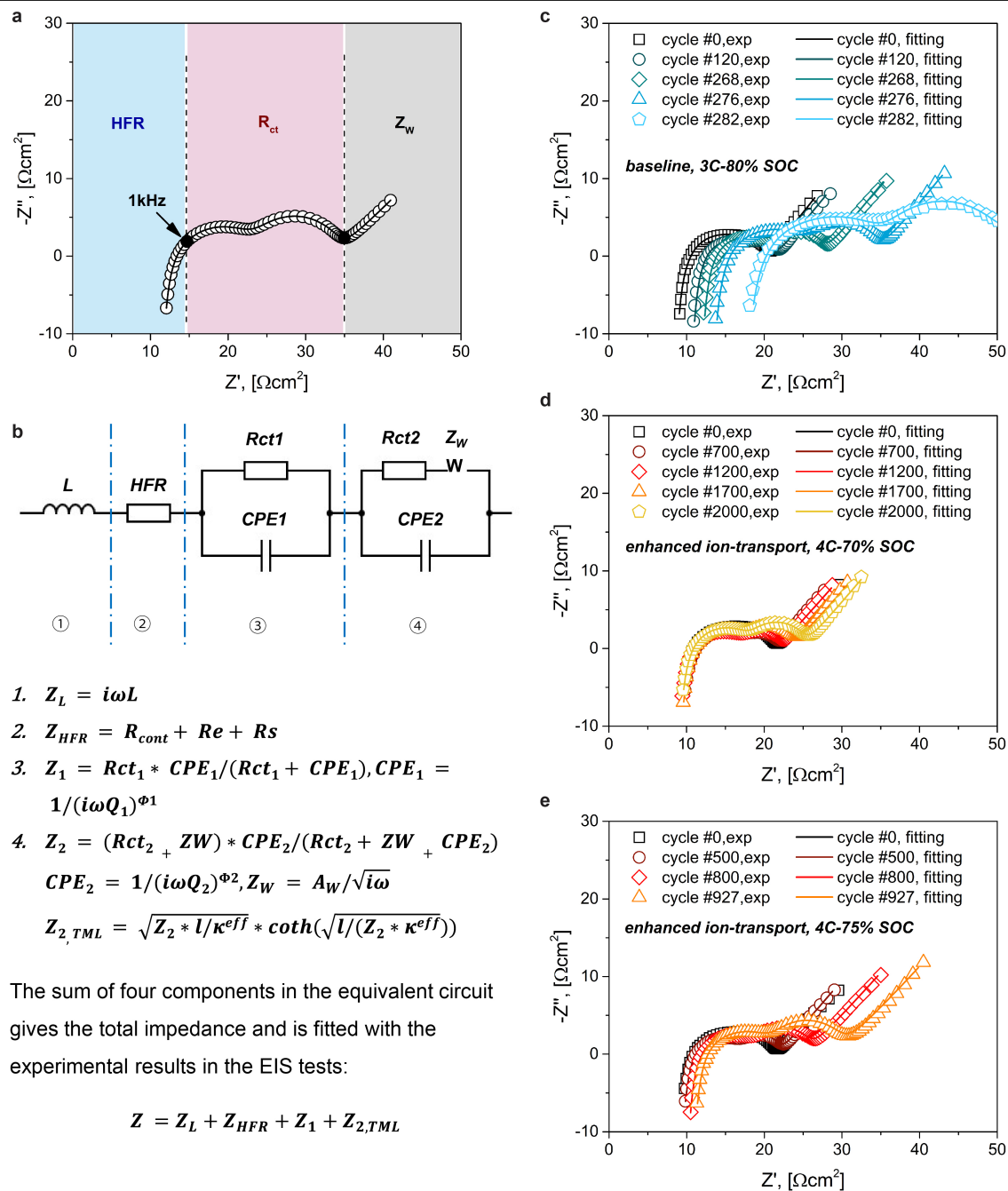
Extended Data Fig. 7 | Parameter map of lithium plating-free (LPF) charging (3.4 mAh cm⁻²). **a**, Simulated LPF region given by relative ion transport resistance and charge transfer resistance when 3C charging the battery (*denotes unitless variables, referenced with the properties of a fresh baseline cell charging at 60 °C). **b**, Simulated LPF region given by relative ion transport resistance and charge transfer resistance when 4C charging the battery, in which the open symbol labelled as 65 °C denotes the high porosity anode. **c**, Change of charge transfer resistance during aging attained from EIS tests and analysis. **d**, Change of ion transport resistance during ageing attained from EIS tests and analysis.
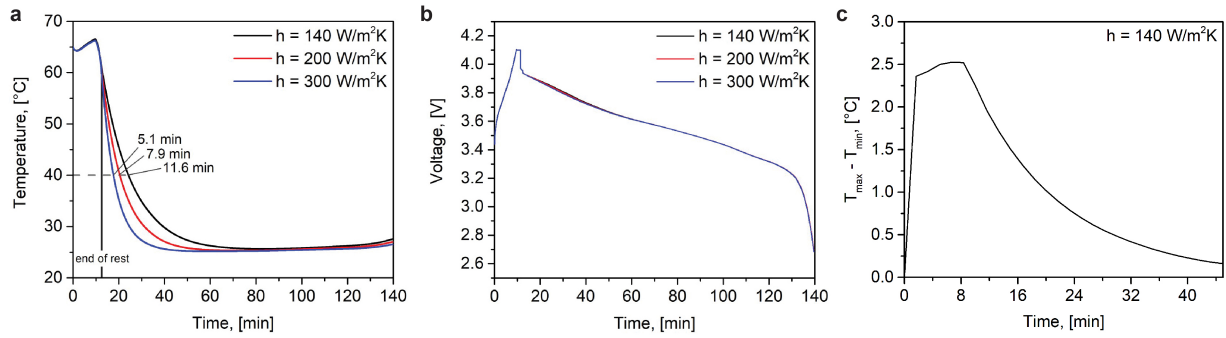
Extended Data Fig. 8 | Effects of heat transfer coefficient. Effects during C/3 discharge on 4C charge - C/3 discharge cycling under otherwise the cooling condition of 140 W per m²K, indicative of dramatic shortening in time for the battery to cool down to below 40 °C. Note that a heat transfer coefficient of 300 W per m²K is still attainable by strong aspirated air convection. **a**, Cell temperature curves. **b**, Cell voltage curves. **c**, Spatial temperature nonuniformity, $T_{max} - T_{min}$, as a function of time.

a, Typical shape and interpretation for cell impedance in the complex plane.

b, Equivalent circuit and the mathematical expression to fit the experimental results.

1. $Z_L = i\omega L$
2. $Z_{HFR} = R_{cont} + R_e + R_s$
3. $Z_1 = Rct_1 * CPE_1/(Rct_1 + CPE_1), CPE_1 = 1/(i\omega Q_1)^{\Phi 1}$
4. $Z_2 = (Rct_2 + ZW) * CPE_2/(Rct_2 + ZW + CPE_2)$
   $CPE_2 = 1/(i\omega Q_2)^{\Phi 2}, Z_W = A_W/\sqrt{i\omega}$
   $Z_{2,TML} = \sqrt{Z_2 * l/\kappa^{eff}} * coth(\sqrt{l/(Z_2 * \kappa^{eff})})$

The sum of four components in the equivalent circuit gives the total impedance and is fitted with the experimental results in the EIS tests:

$$Z = Z_L + Z_{HFR} + Z_1 + Z_{2,TML}$$

Extended Data Fig. 9 | EIS tests and equivalent circuit for fitting. a, Typical shape and interpretation for cell impedance in the complex plane. **b**, Equivalent circuit and the mathematical expression to fit the experimental results. **c**, EIS results and fitting curve for baseline cell under ATM cycling with 3C charging to 80% SOC. **d**, EIS results and fitting curve for cell with enhanced ion-transport under ATM cycling with 4C charging to 70% SOC. **e**, EIS results and fitting curve for cell with enhanced ion-transport under ATM cycling with 4C charging to 75% SOC.